CrossMark

RESEARCH ARTICLE

Eruptive parameters and dynamics of the April 2015 sub-Plinian eruptions of Calbuco volcano (southern Chile)

Angelo Castruccio[1,2] · Jorge Clavero[3,4] · Andrea Segura[1,2] · Pablo Samaniego[5] ·
Olivier Roche[5] · Jean-Luc Le Pennec[5] · Bárbara Droguett[3,4]

Abstract We conducted geological and petrological analyses of the tephra fallout and pyroclastic density current (PDC) products of the 22-23 April 2015 Calbuco eruptions. The eruptive cycle consisted of two sub-Plinian phases that generated > 15 km height columns and PDCs that travelled up to 6 km from the vent. The erupted volume is estimated at 0.38 km^3 (non-DRE), with approximately 90% corresponding to tephra fall deposits and the other 10% to PDC deposits. The erupted products are basaltic-andesite, 54-55 wt.% SiO$_2$, with minor amounts of andesite (58 wt.% SiO$_2$). Despite the uniform composition of the products, there are at least four types of textures in juvenile clasts, with different degrees of vesicularity and types and content of crystals. We propose that the eruption triggering mechanism was either exsolution of volatiles due to crystallization, or a small intrusion into the base of the magma chamber, without significant magma mixing or with a magma compositionally similar to that of the residing magma. In either case the triggering mechanism generated convection and sufficient overpressure to promote the first eruptive phase. The start of the eruption decompressed the chamber, promoting intense vesiculation of the remaining magma and an increase in eruption rate towards the end of the eruption.

Introduction

Calbuco volcano is an active, hazardous volcano located in the Southern Andes of Chile (Stern et al. 2007) that lies 30-32 km E of the cities of Puerto Montt and Puerto Varas (Fig. 1). During the afternoon of 22 April 2015, Calbuco volcano started a new eruptive cycle following only minor precursory activity, which comprised mainly a seismic swarm 3 hours before the start of the eruption (Valderrama et al. 2015); the eruption then generated two successive sub-Plinian phases in 12 hours. These phases produced >15 km high eruption columns with their associated fall deposits to the NE, and pyroclastic density currents (PDCs) that travelled up to 6 km from the vent over most of the flanks of the volcano (Fig. 1). Primary and secondary lahars were also generated on the S, N and NE flanks during and following the eruptions. Airborne tephra caused disruption of flights in the Chilean and Argentinean airspace. In proximal areas tephra fall most strongly affected the people of Ensenada (Fig. 1), a small village located 10 km NE of the volcano summit. After the two main sub-Plinian events, weak activity continued for a couple of weeks until the first half of May, before returning to baseline levels.

✉ Angelo Castruccio
acastruc@ing.uchile.cl

1   Departamento de Geología, Universidad de Chile, Santiago, Chile

2   CEGA (Centro de Excelencia en Geotermia de los Andes), Santiago, Chile

3   Amawta Geoconsultores Ltda., Santiago, Chile

4   Escuela de Geología, Universidad Mayor, Santiago, Chile

5   Laboratoire Magmas et Volcans, Université Blaise Pascal-CNRS-IRD, OPGC, 6 Avenue Blaise Pascal, TSA60026-CS60026, 63178 Aubière, France

Fig. 1 Location map of Calbuco volcano and distribution deposits from fallout, PDCs and lahars of the 22-23 April 2015 eruption. Red dots with numbers indicate the location of the stratigraphic sections
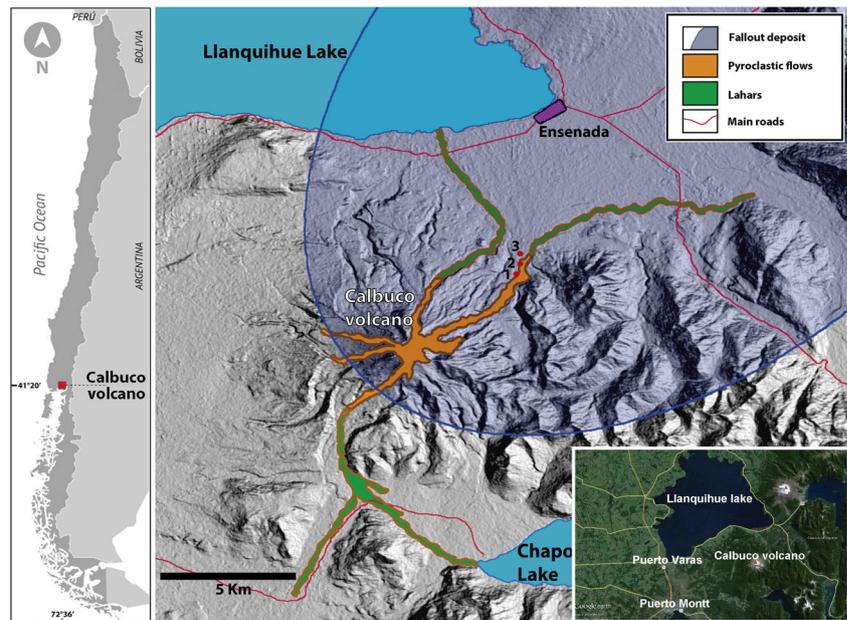
In this article we report results of a comprehensive study focusing on the products emitted during the two sub-Plinian events. We focus on the stratigraphy and regional distribution of the main fallout and PDC units, characterization of eruptive dynamics in terms of volume and intensity of eruptive phases, and the main petrologic features of eruptive products. In a recent paper, Van Eaton et al. (2016) presented satellite observations of the eruption that agree with our interpretation of the timing of the deposits. In another recent work, Romero et al. (2016) presented the first analysis and results on the tephra fall deposit of the eruption. Although their volume estimates coincide with those of this study we interpret the timing and nature of the activity differently. Furthermore we present the first stratigraphic studies on the PDC deposits and characterize the juvenile material of both fallout and PDC deposits (mineral chemistry, whole-rock major and trace elements, SEM analyses). These results provide insights into the eruption style and its possible triggering mechanisms.

Geological setting

Calbuco volcano (41°S, 2,003 masl) is located in the Southern Volcanic Zone (SVZ, Fig. 1) of the Andes and has been one of the most active and hazardous Chilean volcanoes during historical times (since the XVII century). Eruptive activity started at ~300 ka (Sellés and Moreno 2011) and was mainly characterized by effusion of andesitic lavas and domes and their associated PDCs, mainly block-and-ash flows, as well as "cold" and "hot" lahars (López et al. 1992; Castruccio et al. 2010; Sellés and Moreno 2011; Castruccio and Clavero 2015). Holocene products are better preserved and also include sub-

Plinian to Plinian fall deposits and a basaltic-andesite ignimbrite emplaced at about 6.5 ka (Sellés and Moreno 2011). A distinctive hummocky terrain on the lower northern flank is the result of two sector collapses that occurred in postglacial times (Clavero et al. 2008). Historical activity (Petit-Breuilh 1999) includes sub-Plinian eruptions (1893-1895; 1929 and 1961) and other less powerful, Vulcanian eruptions (1906-1907, 1917, 1932, 1945 and 1972).

Chronology of the 22-23 April 2015 eruption

Calbuco volcano started a new eruptive cycle on 22 April 2015 at 18:05 local time. It is interesting to note that on 27 May 2014, a VT event of local magnitude M_l=3.0 was recorded at 16 km depth beneath the volcano (SERNAGEOMIN 2014a). The seismic network of Calbuco consisted of two seismometers located 5-6 km away from the summit and one infrared camera. Regional seismic reports (Valderrama et al. 2015) indicated a rise in the number of low local magnitude (M_l<0.9) volcano-tectonic (VT) events beneath the volcano during the 3 months before the eruption. In December 2014 seismic stations recorded 5 events (4 VT and 1 Long-period – LP) and only 4 in January. During February there was an increase in the number of events (40) and during March 57 events were recorded (SERNAGEOMIN 2014b, 2015a, b, c). Then, three hours before the beginning of the eruption there was a notable increase in shallow seismicity below the volcano, with the occurrence of more than 200 VT and LP earthquakes (SERNAGEOMIN 2015d). Seismic activity and underground noises were felt and reported by inhabitants near

the volcano (5-10 km away from the volcano summit) for a few hours before the eruption.

The eruption started suddenly with the emission of an eruptive column from the summit crater of the volcano, which reached a height of approximately 15 km within a few minutes (Fig. 2a, b). This first eruptive phase lasted ~1.5 hours, with plume dispersion to the NE (SERNAGEOMIN 2015e, f). Occasional, minor column collapses (Fig. 2a) were reported on all flanks of the volcano (Mella et al. 2015), together with the occurrence of primary lahars on the S flank. After the end of this first phase (~19:35 local time, reported visually and seismically), continuous harmonic tremor activity was reported starting at 21:55 local time (SERNAGEOMIN 2015g). On 23 April at 01:00 local time, a second eruptive phase started with the generation of an eruptive column that reached a maximum altitude of 17 km (estimated with satellite images, SERNAGEOMIN 2015h, i, Bertin et al. 2015, Van Eaton et al. 2016). This phase lasted about 6 hours with similar plume dispersion to the NE as the first phase. As this second phase occurred during the nighttime few visual observations were possible, although the lower part of the eruptive column was partially observable due to incandescence at the vent and very intense lightning inside the column (Fig. 2c). We could observe directly that the intensity of both incandescence and lightning varied during this second phase, with a notable increase after 3:30 local time, which coincides with observations made by Van Eaton et al. (2016). These authors attribute this increase to a major occurrence of PDCs. Towards the end of this second phase (~7:00 local time, noticed seismically and by the lack of incandescence and lighting), there was a notable increase in the occurrence of VT events, with a maximum magnitude of 3.2 (Valderrama et al. 2015).

During the two eruptive phases, PDCs reached 6 km from the vent on the NE and SW flanks, and subsequent lahars reached Chapo Lake on the S flank (Fig. 1) where a number of houses and fish farming buildings were destroyed (SERNAGEOMIN 2015i). As a consequence of these two eruptions, air traffic was disturbed in southern Chile and Argentina. The town of Pucón located 230 km to the N (Fig. 1) was completely darkened during the morning of 23 April (6:00-12:00 local time, reported by local inhabitants). Fall deposits blocked the main roads up to 25 km NE of the volcano and many minor buildings collapsed due to the load of tephra (15-40 cm thick) accumulated on their roofs.

In the next days activity decreased notably, with sporadic eruptive events that generated weak plumes (< 2 km high above the vent) and minor column collapses. On 30 April, at 13:08 local time, a third phase occurred, but it was of much lower intensity and magnitude than the previous two. It lasted only a couple of hours, with a 3-5 km high eruption column above vent and a SE dispersion axis (SERNAGEOMIN 2015j). In the following weeks the eruptive and seismic activity decreased gradually, and on 28 May the alert level from SERNAGEOMIN was lowered to baseline, pre-eruption levels.

Methods

Fall deposits at proximal to medial distances (up to 50 km from the vent) were analyzed in the field on 23-25 April and 19-24 May 2015. We did not notice significant compaction of the deposits between these two periods. We sampled 57 sites in proximal and medial areas (5 – 100 km from vent) along the main roads to the NE of the volcano in Chile. No sample site was closer than 5 km from the vent because of safety reasons and difficulty of access.

In order to reconstruct the isopachs and isopleths, we measured the thicknesses of the whole fall deposit and report the

Fig. 2 a Start of the first phase at 18:05 of 22 April 2015. Notice the pyroclastic flows at the base of the developing eruptive column. Picture taken from the N of the volcano (photo by Lester Acuña). b 15-16 km high eruptive column of the first phase. Osorno volcano to the left. Plume dispersion is to the NE. Picture taken from Puerto Varas, 30 km W of the volcano. c Second phase on 23 April. Notice the incandescence and lightning inside the column. Picture taken from Frutillar, 40 km to the NW of the volcano at 2:15 AM
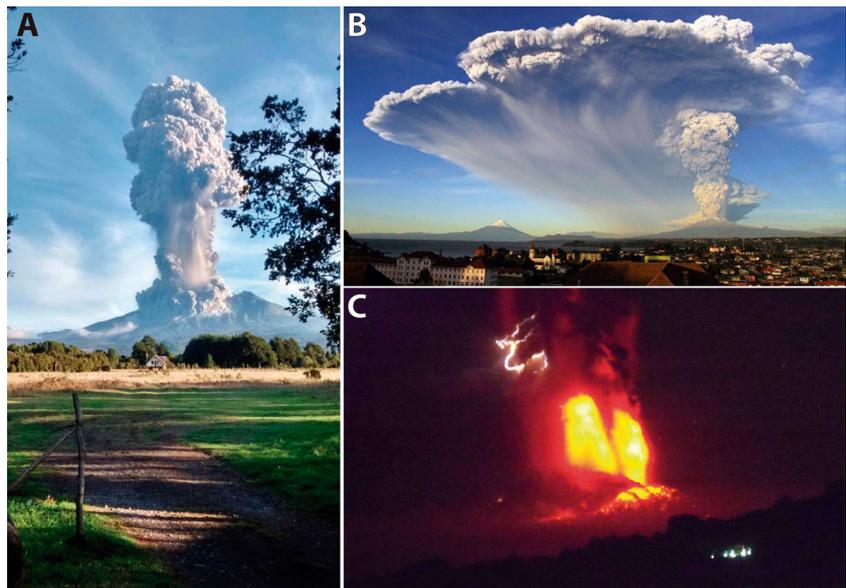
maximum size of clasts in the coarsest layers in the fall deposit by averaging the lengths of the 3 orthogonal axes of the 5 largest clasts for each measurement sample location.

We analyzed 10 tephra fall samples from 3 outcrops along the downwind axis at 6, 14 and 27 km from the vent for componentry and grain-size analysis. For each sample we determined the mean size and sorting parameters (Inman 1952). Additionally, we analyzed the componentry in the 0.5-1 and 2-4 mm size range, separating the different types of clasts with the aid of a binocular magnifying lens and weighing each class. We also made density measurements on selected clasts by determining weights in air and water (Archimedes principle) using clasts sealed in wax.

We conducted a series of petrographic and chemical analyses of the juvenile material. Major elements of mineral and matrix glasses of 7 selected samples from the fallout and PDC deposits were analyzed at Laboratoire Magmas et Volcans (Université Blaise Pascal, Clermont-Ferrand, France) using a CAMECA SX-100 microprobe. The operating conditions were 15 kV accelerating voltage, 10–12 nA beam current, and 10 s counting time for minerals; and 15 kV accelerating voltage, 8 nA beam current, 5-10 μm beam size and 10 s counting time for matrix glass measurements. Major and trace element concentrations of 18 samples from juvenile blocks and bombs of the PDC and the tephra fall deposits were analyzed at the Laboratoire Domaines Océaniques (Université de Bretagne Occidentale, Brest, France). Chemical analyses were obtained by ICP-AES (Inductively Coupled Plasma-Atomic Emission Spectroscopy).

Products of the April 22-23, 2015 eruptions on the NE flank

General stratigraphy

The 22-23 April eruptions generated a series of fallout, PDC and lahar deposits distributed on various flanks of Calbuco (Fig. 1). The tephra fall deposits were distributed mainly to the NE of the volcano, with a total thickness of 52 cm at 6 km from the vent (Fig. 3a) that thinned to 5 cm at 27 km along the downwind axis. We identified four subunits in the fall deposit: layers 0, 1, 2 and 3 from base to top (Fig. 3a, b, Table 1). The deposits contain mainly juvenile basaltic andesite clasts (54.5 – 55.4 wt.% SiO_2) with minor amounts (< 10 vol.%) of lithics. The two lower layers (0 and 1) are composed mainly by brown, vesicular scoria (Fig. 4a). The upper layer (3) is dominated by dark grey, dense scoria (Fig. 4b), while layer 2 is a mix of both types. A third type of juvenile clast is a more vesicular white pumice that makes up < 1 vol.% of the deposit (Fig. 4c, Table 1).

Fig. 3 a 4 layers of the tephra fall deposit, 52 cm thick 6 km NE of the crater. b Tephra fall deposit, 23 cm thick 16 km from the vent. c Río Blanco-Frío valley, one month after the eruption; note strong smoking from the PDC deposits, which had been eroded by secondary lahars. Locations of stratigraphic sections indicated d PDC lobe (unit I) from the second phase of the eruption. Notice the concentration of scoria bombs at the front. Layer 3 of the fall deposit partially covers the lobe. e PDC deposit layer C. Notice the undular contact with deposit D (above) and the abundance of whitish, highly crystalline blocks (WB) and cauliflower scoria bombs (CB). Shovels for scale. f detail of sharp contact (dashed line) between 2 pyroclastic density current beds; the upper contains brown scoria fragments incorporated from the lower one (BS). A "cauliflower" scoriaceous bomb (CB) is also shown
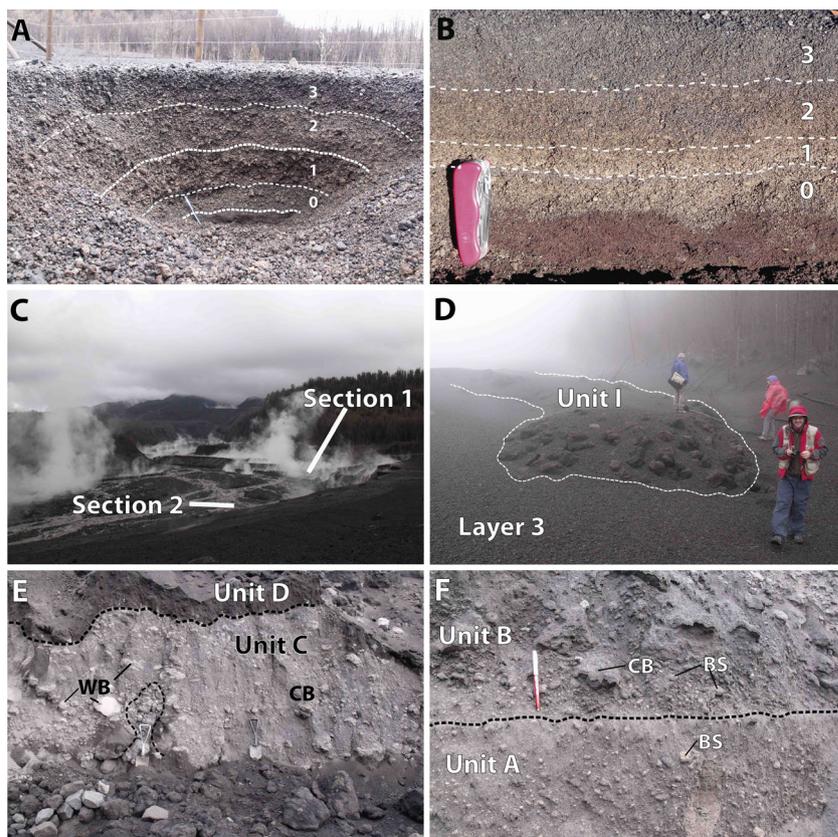
Table 1 Field description of the stratigraphic units of the 22-23 April 2015 Calbuco eruption

Unit	Type of deposit	Description
0	Fallout	basal unit. It rests directly on pre-eruption soil or bedrock. It has a maximum measured thickness of 8 cm at 6 km from the vent (Fig. 3a). It can be distinguished only within the first 20 km from the vent and it contains brown scoria fragments as well as reversely graded lithics and dark-grey dense juvenile fragments. It is the unit with the highest lithic proportion (~10 %). In some medial sectors (~15 km from the vent) the enrichment of dark-grey dense juvenile clasts towards the top of this unit forms a distinct layer (Fig. 3b). Juvenile fragments are scoriaceous, sub-equant, subangular, and light brown in colour. Vesicles (30-60%) are mostly spherical and up to 1 cm in diameter depending on the size of the fragment. Phenocrysts (<10 %) are mainly plagioclase and pyroxene with a euhedral form and up to 1-2 mm in size, within a glassy semi-vesicular groundmass (50-60%). Dense juvenile clasts are dark grey, subangular and have up to 15% phenocrysts (mainly plagioclase and pyroxene) within a microcrystalline groundmass. Vesicles (15-20 vol.%) are sub-rounded which are smaller (<1-2 mm) than those in brown scoria fragments (Fig. 4b). Lithics are mainly dark grey angular lava fragments with different degrees of oxidation or alteration.
1	Fallout	This unit has a maximum measured thickness of 15 cm at 6 km from the vent and contains the largest brown scoria fragments of all the layers, with mean clasts diameter of >7 cm at 5 km from the vent. Clasts are mainly brown scoria (fig. 4a) with subordinate dark-grey dense juvenile fragments (fig. 4b). The deposit shows reversely-graded lithics and juvenile fragments. Scoria fragments have the same petrographic features as in layer (0).
2	Fallout	This unit has a maximum measured thickness of 20 cm at 6 km from the vent. The layer is mostly massive, with a normal grading of lithics and juveniles only at the base. It is characterized mainly by brown scoria and an increasing presence of grey dense juvenile fragments towards the top. Scoria fragments have mineralogical assemblages, textures and vesicularities similar to those in layers (0) and (1).
3	Fallout	This unit has a maximum thickness of 9 cm at 6 km from the vent. It shows a reverse grading of clasts, with an almost completely absence of fine ash at the top. It has a distinctive dark grey color, due to a very high proportion (>80%) of dark grey dense juveniles. It also contains grey lithics and scarce (<5%) highly vesicular whitish pumices. Highly vesicular (60-90% vesicles) whitish pumices are subangular with more fibrous vesicles and a different mineralogy compared with the scoria as they contain scarce amphibole in addition to plagioclase and pyroxene phenocrysts (Fig. 4c).
A	PDC	PDC unit deposited on top of fallout layers 0 and 1 (Segura et al. 2015; Clavero et al. 2015) or on top of pre-2015 lahar deposits or bedrock. It is up to 2 m thick and contains abundant (10-35 vol.%) brown vesicular subrounded scoria within a consolidated fine-grained massive ash matrix. The unit has gas segregation pipes cut by the overlying deposit. Scoria are <8 cm in diameter, with crystals of plagioclase and pyroxene, similar to those of brown scoria from the fallout deposit.
B	PDC	PDC unit with a sharp subhorizontal basal contact with PDC unit A below (Fig. 3). The unit is up to 80 cm thick. It has gas segregation pipes cut by the overlying deposit, PDC unit C. It contains cauliflower dark-grey scoriaceous bombs up to 25 cm diameter as well as brown scoria at its base incorporated from unit A (Fig. 3f), within a semi-consolidated fine ash matrix. Locally, it shows a laminated fines-depleted base (<20 cm thick).
C	PDC	PDC deposit up to 2.8 m thick with undulated basal and upper contacts interpreted as erosional structures (Figure 3e). This unit distinguishes from the rest by the presence of highly-crystalline (50-90 vol.% crystals), whitish prismatically jointed blocks (PJB, Fig. 6b) fragments up to 25 cm diameter. These whitish fragments are the only juvenile products of the eruption with an andesitic composition. Some PJBs show scoriaceous and glassy bands with undulating contacts. It also contains large cauliflower scoriaceous bombs up to 80 cm in diameter, and glassy black clasts (up to 15 cm diameter) within an unconsolidated, massive gray matrix composed of medium ash to fine lapilli.
D	PDC	PDC deposit up to 1.5 m thick with undulated (deformed) base and subhorizontal upper contact. It contains cauliflower scoriaceous bombs (<40 cm in diameter), subangular lithic fragments (<20 cm diameter) within a massive, medium to coarse ash, greyish to reddish matrix.
E	PDC	PDC deposit up to 2.5 m thick containing two sub-units. The lower (E1) sub-unit shows well-developed lamination, cauliflower bombs up to 40 cm in diameter and lithic fragments (diameter <35 cm) within a fine-to-medium ash, crystal-rich matrix with carbonized material. The upper sub-unit (E2) has well-developed laminated 2-10 cm thick layers formed by fine-to-medium lapilli with some scoriaceous bombs (up to 23 cm in diameter).
F	PDC	Massive PDC deposit with abundant cauliflower scoriaceous bombs up to 60 cm in diameter, subrounded lava lithics (up to 1.4 m in diameter) within a-fine-to medium ash matrix. It contains large carbonized to semi-carbonized tree trunks from previously untouched forested terrain. Locally there are lenses of high concentrations of accidental lithics and bombs that are almost clast supported.
G	PDC	Layered PDC deposit with 3 distinct subunits. The lower one, up to 20 cm thick, is a fines-depleted layer containing polylithologic, lithic-rich, fine lapilli fragments. The intermediate layer, up to 6-cm thick, contains a discontinuous non-carbonized vegetation-rich paeleosoil horizon deformed and incorporated by the flow. The upper layer, up to 2.5-m thick, has an undulated upper surface and contains large cauliflower bombs up to 1.1 m in diameter and subrounded lithic fragments up to 1.2 m in diameter within a massive, fine-to-medium ash matrix. Large bombs and lithics increase in size towards the top of the deposit.
H	PDC	Unit formed by two distinct units up to 25 cm thick in total and separated by a discontinuous thin laminated ash layer (<1 cm thick). The lower unit (H1) is a fines-depleted, polylithologic, well-sorted, fine-to-medium, lapilli slightly laminated layer. The upper unit (H2) is a fine ash, crystal-rich layer with dispersed (15% vol.) large lithic fragments (up to 15 cm in diameter) concentrated towards the upper part of the deposit. It is partially overlain by layers 2 and 3 of the fall deposit.

Table 1 (continued)

Unit	Type of deposit	Description
I	PDC	PDC deposit that tops the entire sequence of PDCs and is characterized by flow units with lobe morphology, with terminal fronts that are 5 m wide and 1-2 m thick and with well-developed levées. Both the front and lateral levées are rich in scoria bombs up to 50 cm in diameter (Fig. 3d, 6a), some of which contain enclaves and layering (Fig. 6c, d). The deposit is mostly massive, with occasional lenses (1 m thick, ~5-6 m length) rich in scoria bombs with cauliflower morphology and up to 60 cm in diameter. The matrix is composed of medium grained ash. This unit is overlain by the entire layer 3 of the fallout deposit.

PDCs were generated in some of the main valleys and gullies around the volcano, reaching up to 6 km from the vent (Fig. 3c, d, e, f). We investigated in detail the PDC deposits located in the Frio-Blanco-Hueñu Hueñu river system on the N and NE flanks of the volcano. At least 8 successive pyroclastic density currents inundated parts of the Río Frio and Río Blanco valleys (Units A to I from base to top, Fig. 5, Table 1). Individual deposits have thicknesses of 2-4 m, while the whole sequence has a thickness of 20-30 m. These PDC deposits were emplaced above the two lower tephra fall layers (0 and 1) and below the upper fall deposit layer (layer 3, Fig. 5).
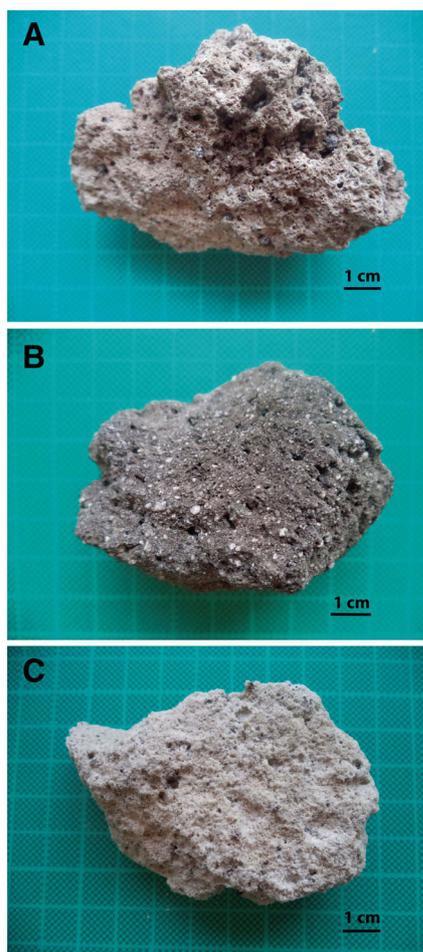
Fig. 4 **a** Brown Scoria from fall deposit layer 1. **b** Dark-grey, dense juvenile from fall deposit layer 3. **c** White, highly vesicular pumice from fall deposit layer 3

The PDCs are partially eroded (and dissected) by a series of secondary lahar deposits, forming a pyroclastic terrace in the valley, situated 20-30 m above river level.

Most of the PDC deposits observed on the NE flank are massive and rich in dense scoria bombs (Fig. 6a), although some units present diverse sedimentary structures (Table 1). Individual deposit units have a levée-channel morphology, with lateral margins and frontal lobes enriched in bombs up to 1 m in diameter (Fig. 3d). This is typical of pyroclastic flows in which grain size segregation causes concentration of coarse clasts at the top and margins, the latter forming static levées that delimit a central channel from which most material is drained and finally accumulates at the front to form the frontal lobe (e.g. Jessop et al. 2012).

Deposit C (Fig. 3e) contains a predominance of whitish, highly crystalline dense clasts (Fig. 6b) that were not recognized in any other deposit and have a different composition (andesitic, 58 wt.% SiO_2) compared with the rest of the eruption products. There are also occasional clasts with enclaves and mixing textures in all units (Fig. 6c, d).

Distribution, volume and eruptive parameters

The tephra fall isopachs maps (Fig. 7a, b) show distribution mainly to the NE, with a main axis at ~N35°E, which is consistent with satellite observations of the plume dispersion during the eruption (Fig. 7e). Calculation of the deposit volume for each layer was not straightforward, mainly because it was not possible to identify individual layers in distal areas. We estimated the total volume of the two eruptive phases using the isopachs of the whole deposit (Fig. 7a, b), considering the exponential (Pyle 1989; Fierstein and Nathenson 1992), power-law (Bonadonna and Houghton 2005) and Weibull (Bonadonna and Costa 2012) methods (Fig. 7f). The exponential method with two segments gives a total bulk volume of 0.29 km^3; the power law method, 0.28 km^3 (using a distal integration limit of 400 km); and the Weibull fit, 0.38 km^3 (see discussion for these differences and comparison with Romero et al. 2016).

According to the higher intensity of the second phase (Van Eaton et al. 2016), the relative thickness of each fall deposit layer, the timing of the PDCs and the correlation between fallout and PDC deposits, we assign layer 0 to the first phase and layers 1, 2 and 3 to the second phase. Romero et al. (2016)
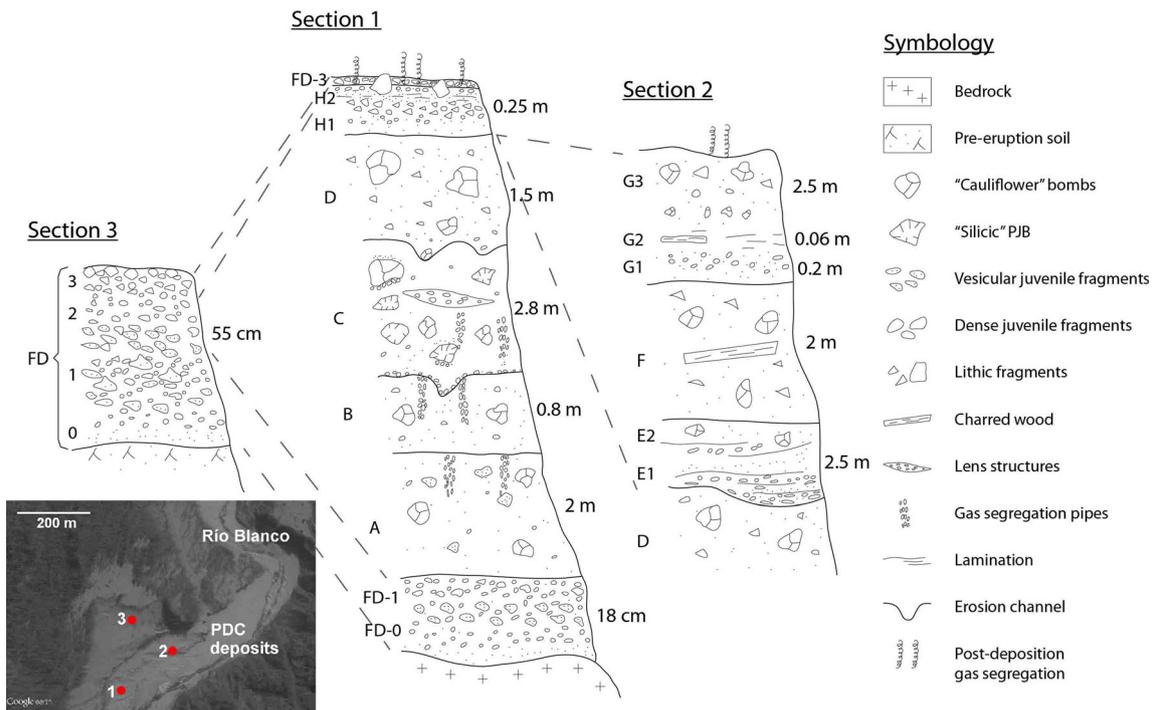
Fig. 5 Stratigraphic scheme (not to scale) of 3 sections in the Río Blanco – Frío valley, showing the relationships between the tephra fallout and PDC deposits. Map insert indicates the location of each section

assigned layers 0 and 1 (units A and B in their work) to the first phase, but they did not consider the stratigraphic relationships between the PDCs and fall deposits. Furthermore, their eruption rate results indicate a nearly constant intensity through both main phases, whereas Van Eaton et al. (2016) clearly indicate a higher intensity for the second phase. We used proximal thicknesses to estimate the respective volumes of the first (layer 0) and second (layers 1, 2 and 3) eruptive phases at approximately 15% and 85% of the total erupted volume.

Figs. 7c and 7d show the reconstructed isopleths for layers 1 and 3. For layers 0 and 2 it was not possible to reconstruct isopleths as these units were not easily recognizable in medial and distal parts. Using the method of Carey and Sparks (1986), the estimated maximum column heights corresponding to these layers were 16.5 and 17 km above the vent, respectively, in agreement with satellite estimations of the second phase (Van Eaton et al. 2016). The maximum mass eruption rates estimated from these column height values according to Wilson and Walker (1987) are 2.4×10^7 kg/s and 2.7×10^7 kg/s.

The area covered by the PDC deposits on the NE flank is approximately 650,000 m^2. Assuming a mean thickness of 15 m

Fig. 6 **a** Dark-grey dense bomb from the upper unit I of the PDCs. **b** Whitish, highly crystalline bomb from the C unit of the PDC deposits. **c** Bomb from unit I of the PDC deposit. Notice layering with darker zones, with texture similar to scoria bombs. **d** Scoria bomb from unit T, with whitish, highly crystalline enclave
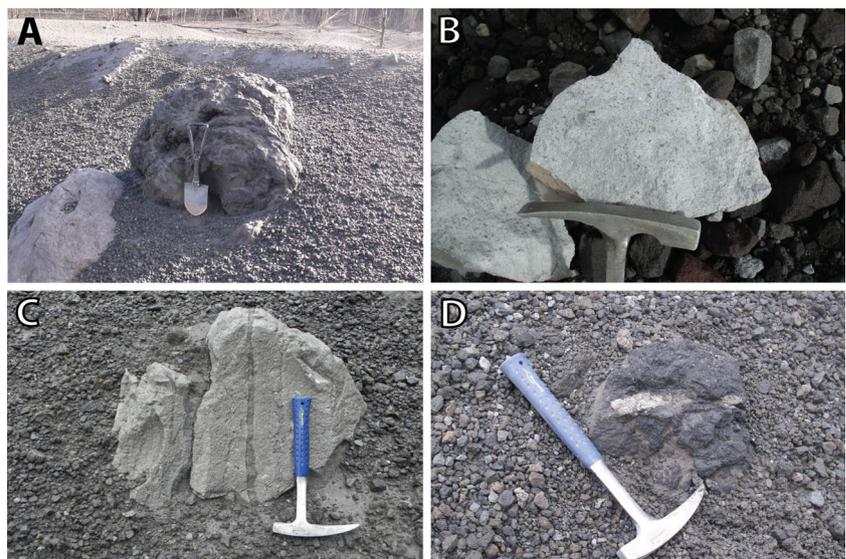
Fig. 7 a Proximal isopachs (in cms) of the 22-23 April eruptions (total deposit). **b** Distal isopach (0.1 cm) of the total deposit. **c** Isopleth (in cm) of layer 1. **d** Isopleth (in cm) of layer 3. **e** Satellite image (from NASA) showing the plume dispersion of the second phase. **f** Thickness versus square root of area of the total (phase 1 + 2) fall deposit from the eruptions with Weibull, power law and exponential fits
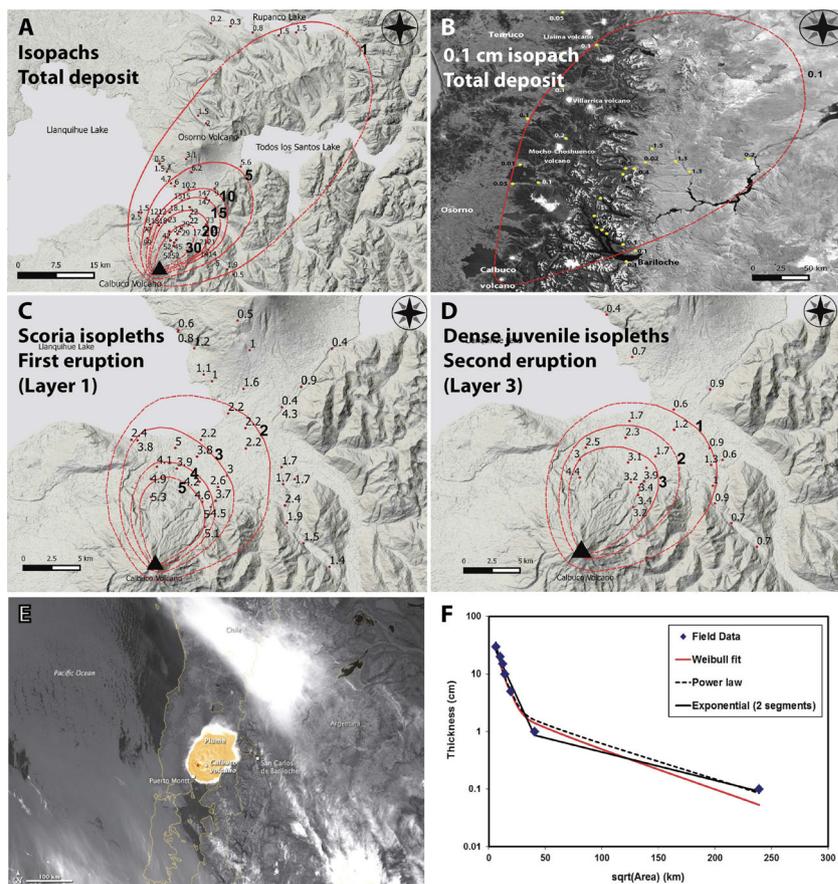
for the whole sequence, a volume of ~10^7 m^3 is obtained in this sector and ~3×10^7 m^3 (i.e. 0.03 km^3) for the whole deposit, equaling less than 10 vol.% of the fall deposit volume. Taking into account the individual thicknesses measured, it is likely that each individual flow deposit volume is less than 10^6 m^3. Satellite images (Google Earth) show that pyroclastic flow deposits on the W and SSW flank had slightly shorter runouts and probably slightly smaller volumes compared to those of the SE flank.

Componentry and grain size analysis

The componentry of all fall deposit samples is dominated by juvenile material. In the 0.5-1 and 2-4 mm ranges, lithic fragments represent less than 12 wt.% in all layers (Fig. 8a). Layers 0 and 1 are dominated by brown scoria (78 and 90 wt.% at 5 km from the vent and 95 and 96 wt.% at 14 km, respectively in the 2-4 mm range) with low contents of dense, dark grey scoria (10 and 5 wt.% at 5 km and 2 and 1 wt.% at 14 km). Layer 2 has greater abundances of dense dark-grey scoria (25 and 15 wt.% at 5 and 14 km respectively). Layer 3 contains the greatest abundance of dark grey dense scoria (78 – 90 wt.% versus 3 – 20% of brown scoria in the 2-4 mm range).

All fall deposit samples plot in the tephra-fall field defined by Walker (1971), with calculated modes between -3Φ and -2Φ. The sorting of the samples ranges between 1.05Φ and

1.4Φ, indicating well-sorted deposits (Fig. 9a). All samples have very low amounts (< 5 %) of fine material (< 63 μm), except layer 3 which has 6 wt.% of fine material at 6 km from vent (Fig. 8a). All samples are unimodal, with a better sorting and finer grain-size with distance (Fig. 8b).

Grain-size distributions of the PDC deposits are shown in Fig. 9c and d. Most samples are within the dilute and dense PDC fields of Walker (1971), although some units are well-sorted, similar to the fall deposits (Fig. 9a). Most of the samples show modes in the range between -1Φ and 1Φ and standard deviations between 2.5Φ and 4Φ. PDC deposits that are massive (layers A, B, C, F) show two modes, typically at -4Φ and 3Φ (Fig. 9a, b). Laminated PDC deposits are better sorted with only one mode at -1Φ, -3Φ or 5Φ. The componentry of selected samples in the 1 mm range is shown in Fig. 9b. Most of the samples show a similar proportion of brown vesicular and dark grey dense juvenile fragments. The PDC samples show lithic contents in the range of 7 to 43 wt.%, generally much higher than the lithic content of the fall deposit samples (<10%).

Petrological data

There are 4 types of juvenile clasts in the eruption deposits (Table 2). The two most abundant types are brown vesicular

Fig. 8 **a** Componentry in the 4 and 1 mm range of selected samples of the tephra fall deposit. **b** Grain size distribution of the tephra fall deposit samples at 6, 14 and 24 km from the vent
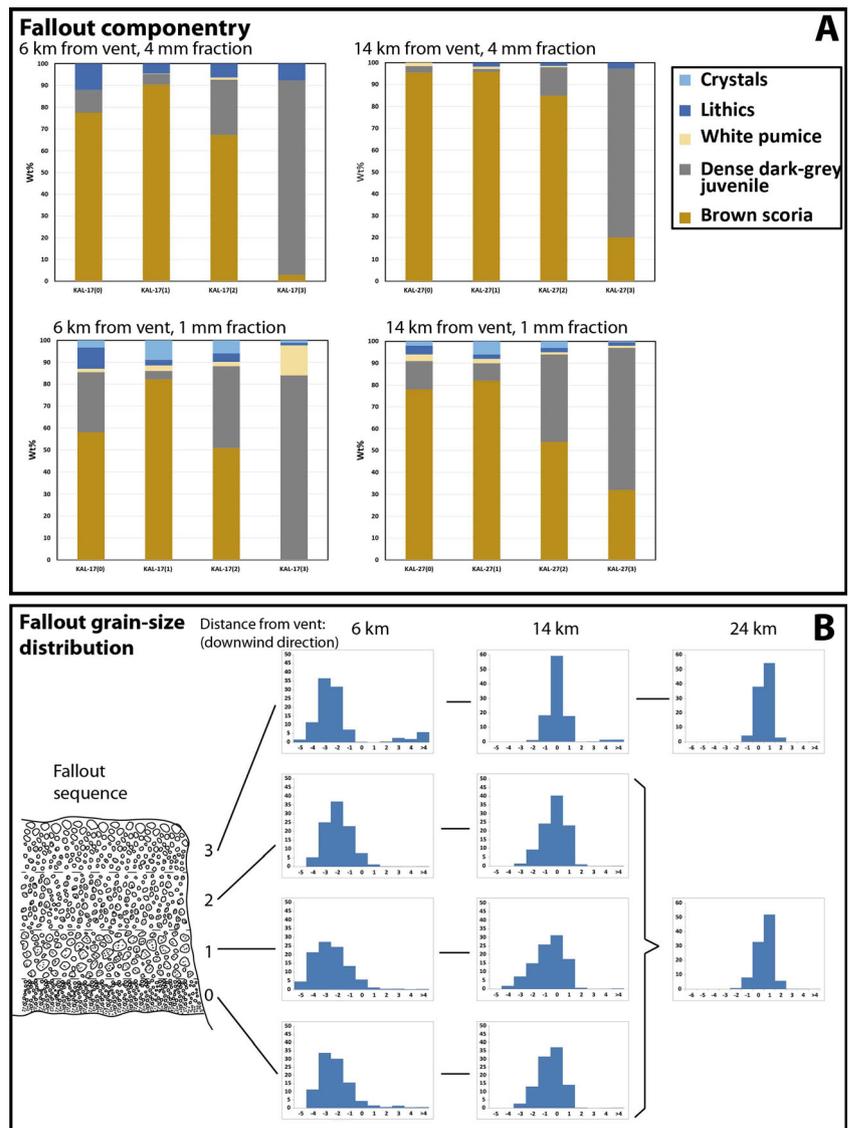
scoria and dark grey, dense scoria. SEM images reveal that brown scoria are more vesicular (30 – 60 vol.% versus 15 – 20 vol.%) than the dense clasts and have fewer microlites (Fig. 10a, b, c, d). Phenocryst content varies between 20 – 25 vol.%, except for whitish clasts from PDC unit C (90 vol.%). Vesicularity varies from <5 vol.% in dense whitish clasts to 90 vol.% in white pumices. The mineralogy of all types of clasts includes plagioclase, ortho- and clino-pyroxene, minor amounts of olivine and Fe-Ti oxides (Fig. 11a, b, c, d, Table 3). Plagioclase is normally zoned with tiny (10-20 μm) overgrowth rims rich in Na. There are also occasional reverse zoned plagioclase crystals (Fig. 11a). White pumice also contain amphibole (Fig. 11c).

All scoriaceous and dense juvenile are basaltic andesite (54.5-56.5 wt.% SiO_2, normalized on an anhydrous basis, Table 4) with similar major and trace element compositions (Fig. 12). Pumiceous samples are slightly more silicic (56.3-56.5 wt.% SiO_2), whereas the whitish, highly crystalline clasts

from PDC unit C are andesitic (58.1 wt.% SiO_2). These samples plot inside the field of Calbuco volcano compositions (López-Escobar et al. 1992; Sellés and Moreno 2011), which define a low-to-medium-K calc-alkaline magmatic series characterized by basaltic andesites and andesites with scarce basalts and dacites (Fig. 12a). The composition of 2015 Calbuco samples is very similar to the 1961 lava flow.

Discussion

Dynamics of the April 2015 eruption and eruptive parameters

The eruption of 22-23 April 2015 consisted of two phases that lasted 1.5 and 6 hours, respectively, with eruptive columns
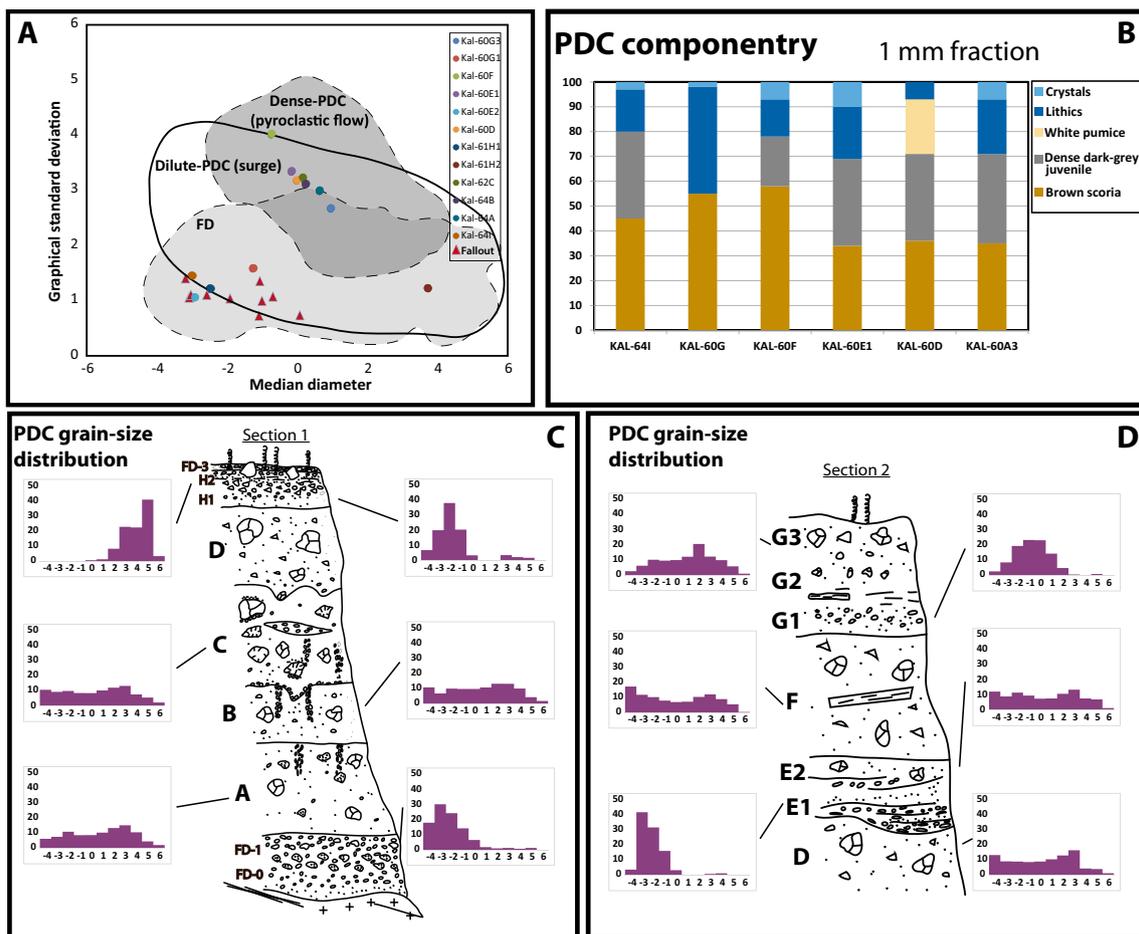
Fig. 9 a Median and standard deviation of fall deposit and PDC samples from the eruption. Fields of fallout, pyroclastic density current and "surge" (dilute PDC) from Walker (1971) are also shown **b** Componentry in the 1 mm range of selected samples of PDC deposits. **c** Grain size distribution of PDC deposits from section 1. **d** Grain size distribution of PDC deposits from section 2

with a maximum height of ~17 km above the crater, and generated PDCs that travelled up to 6 km from the vent, as well as the occurrence of lahars immediately after and during the weeks following the eruption. Visual reports and fall deposit characteristics indicate that the eruptive column during the first phase reached its maximum height very shortly after the start of the eruption and was relatively steady thereafter with little fluctuations. The second phase was more pulsatory and produced larger PDCs, which reached longer distances than during the first phase. We correlate layers 1, 2 and 3 with the second phase. We were unable to estimate column height from layer 2, but its smaller maximum clast size (Fig. 3a, b) suggests a lower column height during the deposition of this layer. We correlated this layer with the major occurrence of PDCs, because layer 0 and 1 are below the PDC units and the entire layer 3 is above. These observations agree with those of Van Eaton et al. (2016), who noted a stopping of the cloud expansion between 2:38 and 3:38 local time, which could indicate a decrease in the eruption rate. They also suggest onset of the major occurrence of PDCs at ~3:00 local time. Our observations indicate that eruption rate increased again at the end of

the eruption, because layer 3 is reversely graded and lacks normal grading towards the top.

Due to the correlation of layer 2 of the tephra fall deposit with the PDC deposits, we suggest that the major occurrence of PDCs during the second phase was associated with eruption of a large proportion of denser clasts (indicated by the PDC componentry, Fig. 9) and partial column collapse, instead of an increase of the eruption rate. Pyroclastic flow deposits represent approximately 10 vol.% of the total eruption volume, indicating that they were a minor product of the eruptive columns compared with fallout.

Bertin et al. (2015) and Van Eaton et al. (2016) estimated a column height of ~ 15 km for the first phase based on the height of the umbrella cloud in satellite images. Our column height estimate for the second phase (~17 km) is similar; although they reported overshooting tops of 23 km. Romero et al. (2016) calculated lower heights for all the tephra fall layers (12 – 15 km). This could be due to uncertainties of clast density and/or size measurements, although Romero et al. (2016) did not recognize the reverse grading observed in layer 3, which could explain their lower value of column height.

**Table 2** Description of the 4 types of juvenile fragments from the eruption

Type of clast	Unit	Description	SiO2 range
Brown socria	Fallout and PDC	Brown vesicular scoria (fig. 4a) fragments present a wide range of bulk vesicularity, ranging from 30 to 60% (Fig. 9a, c, d, 10a, c), with higher vesicularities for larger clasts. Density measurements made on clasts of 4-5 cm of diameter gave values of 1.3 – 1.4 g/cm3. In hand samples vesicles can be up to 1 cm in diameter. SEM images (Fig. 10a, c) reveal different size populations of vesicles ranging from 30 μm to 1 mm. Vesicles are usually sub-spherical, showing signs of coalescence (Fig. 10a, c). These clasts display a porphyritic texture (20-25 vol.% phenocryst), with phenocrysts of plagioclase, orthopyroxene, clinopyroxene and minor amounts of olivine and Fe-Ti oxide. The groundmass is composed of glass and minor amounts of microlites (mainly plagioclase).	54.7 - 55.4%
Dark grey dense	Fallout and PDC	Dark grey, dense (1.6-1.8 g/cm3) scoria presents lower vesicle contents. In hand samples, vesicles are no larger than 3-4 mm. SEM images reveal a vesicle content content of 15-20% and a size range of <0.5 mm to 30 μm (Fig. 9b, c, d). Vesicle form varies from sub-spherical to irregular with less signs of coalescence (Fig. 10) than in the brown vesicular scoria (Fig. 10b). The texture is porphyritic with the same type and content of phenocrysts than brown vesicular clasts. The groundmass is composed of glass and a much higher contents of microlites than brown vesicular scoria (Fig. 10d). Bombs from the PDC deposits are dark grey, poorly to moderately vesiculated (10-25 vol.%) and porphyritic (20-25 vol.% phenocryst). The groundmass shows banding due to different degrees of vesicularity and crystal content, ranging between 10 vol.% in a brownish glass up to 25 vol.% in a clear glass. The latter bands also show glomeroporphyritic textures with plagioclase-orthopyroxene assemblage. The light-colored, sub-rounded magmatic enclaves found in blocks from the PDC deposits display a texture and mineralogy similar to that of the pumice clasts found in the fall deposit.	54.7 - 55.1% in fallout, 55.0 - 55.4% in PDCs
White pumice	Fallout	White pumice clasts (< 1.0 g/cm3) display a glassy texture with vesicle content up to 90%. Vesicles could be spherical or elongated and up to 1 cm length. The glass thickness between vesicles could be < 10 μm. Phenocrysts are 10-15% and microlites are almost absent. Mineralogy is slightly different compared with the other type of clasts and consists of plagioclase, orthopyroxene, amphibole, Fe-Ti oxides, and minor amounts of clinopyroxene.	56.30%
Whitish dense	PDC unit C	Whitish prismatically jointed blocks from unit C of the pyroclastic flows are without vesicles, and are almost completely crystalline (<10% glass) and are the only andesitic products of the eruption. Crystals are up to 1.5 cm in length and correspond to plagioclase, ortho-pyroxene, minor amounts of clinopyroxene and greater amounts of olivine compared with the other juvenile clasts, with minor amounts of Fe-Ti oxides. There is no amphibole in these blocks.	58.10%

The volume of the fall deposits obtained with the Weibull method is considerably larger (~30%, 0.38 km^3) than those obtained with the exponential or power-law methods. This could be due to the lack of very proximal data (< 5 km from the vent), which does not permit us to identify an additional proximal segment in the exponential method. Uncertainty in the total extent of the deposit in distal areas is problematic for the power-law method. The distal fallout in Argentina left a very thin deposit (< 0.5 cm) that was quickly eroded by subsequent rain and wind. According to Bonadonna and Costa (2012) the Weibull function can overcome to some extent problems related to proximal and distal deposits, as it does not depend on integration limits and has fewer fitting parameters.

According to our volume estimations (Weibull method), the first phase emitted ~8 x 10^{10} kg in 1.5 hours, which implies a mean mass eruption rate of 1.4x10^7 kg/s. According to Wilson and Walker (1987) this value implies a mean column height of 14.7 km, close to the value reported by Bertin et al. (2015) and Van Eaton et al. (2016). The second phase emitted ~3.2 x 10^{11} kg in 6 hours, which implies a mean eruption rate of 1.5 x 10^7 kg/s, almost equal to that of the first phase. However, the calculated eruption rate for layers 1 and 3 is ~2.7x10^7 kg/s based on the column height calculated from isopleths. Thus, the eruption rate

Fig. 10 SEM images of the brown scoria (**a** and **c**) and Dense dark-grey juvenile (**b** and **d**) of the tephra fall deposit. Notice the larger size of vesicles in **a**. Dark-grey samples have a higher density of vesicles but of smaller size. Notice in **d** the high content of microlites
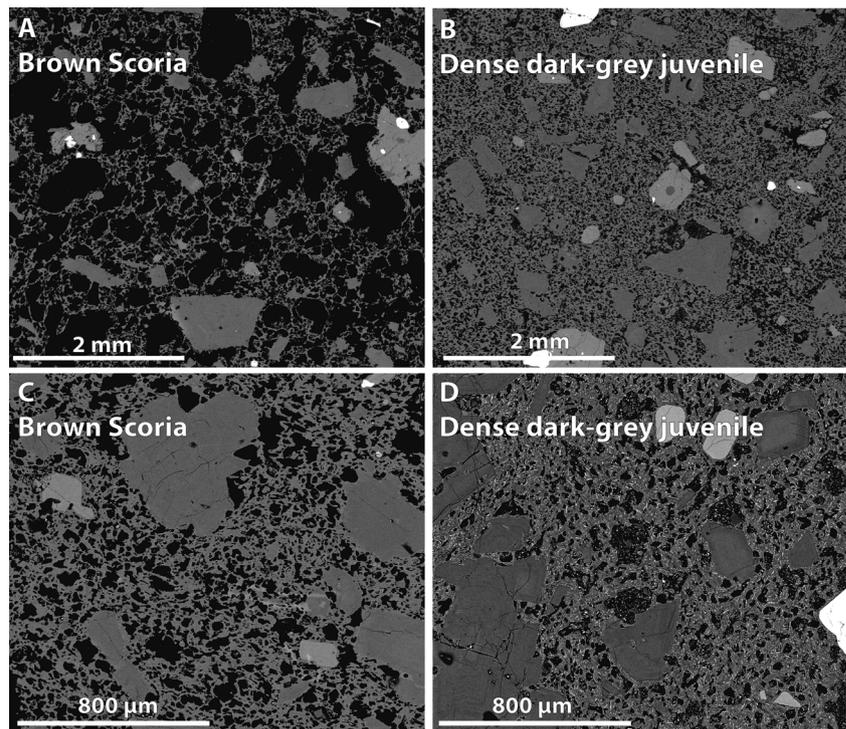
during sedimentation of layer 2 must have been lower, confirming our observations of the tephra fall deposit or alternatively we underestimated the volume of the second phase. Thus, we suggest that a total bulk volume of 0.38 km^3 (0.15 km^3 DRE assuming a deposit density of 1,000 kg/m^3) is probably the best estimate and it is close to the estimate made by Van Eaton et al. (2016) of 0.58 km^3. The eruptive volume classifies the eruption as a VEI 4 (Newhall and Self 1982) with an intensity of 10 and

magnitude of 4 (Pyle 2000); both phases of the eruption are classified as sub-Plinian in agreement with Romero et al. (2016).

Layer 3 is noteworthy for the dominance of dense, dark grey juvenile clasts, as opposed to the more-vesicular and brown clasts that are dominant in the rest of the fall deposit (except at the top of layer 0 which is also enriched in dense juvenile clasts and indicates the end of phase 1). That layer 3 also has slightly higher content of fine-grained tephra might suggest a higher degree of

Fig. 11 Microprobe images of selected minerals from fragments in tephra fallout and PDC deposits. **a** Plagioclase with oscillatory zonation in rims **b** Ortho and clino-pyroxene from brown scoria. **c** Amphibole from white pumice **d** olivine from sample of C unit of the PDC deposit
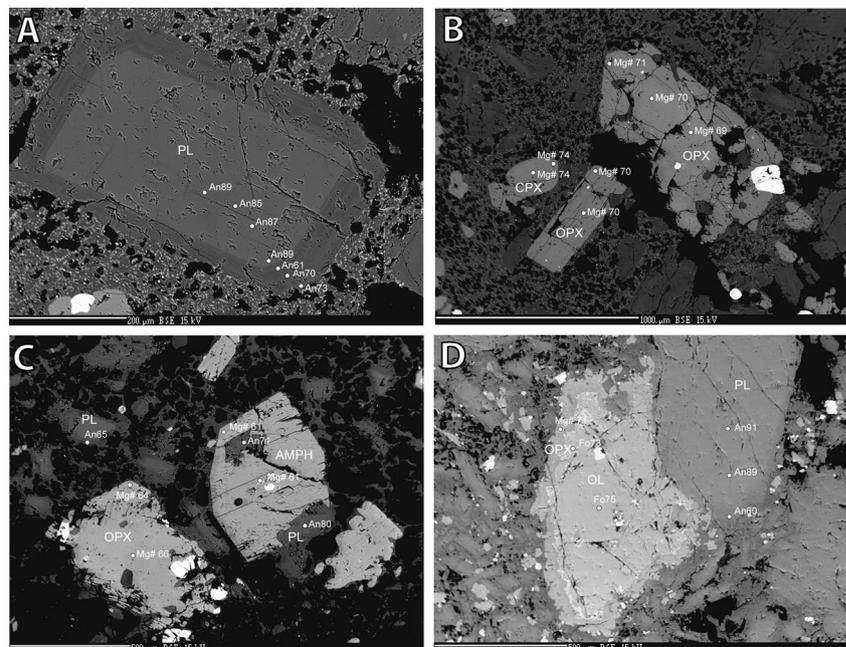
Table 3 Main features of the mineral phases of the products of the Calbuco eruption

Mineral phase	Description
Plagioclase	is the most abundant phenocryst phase (53-70 vol.%; 0.2-2.5 mm) and appears as euhedral phenocrysts, microphenocrysts and microlites. It shows a wide compositional range from An54 to An91. Most phenocrysts appear as clean (non-altered) crystals that display strong normal zoning patterns (Fig. 11a), with core (and interior parts) ranging from An68 to An91, and commonly showing 20-40 μm-width overgrowth rims of Na-rich compositions (An54-75). In the whitish blocks from PDC unit C only, a second, minor population consists of the rare euhedral phenocrysts with sieve-textured concentric zone and cores of Ca-rich composition.
Orthopyroxene	18-22 vol.%, 0.1-2.0 mm in size. Crystals are euhedral with homogeneous composition that corresponds to the enstatite field (En61-70, Fs27-36, Wo2-4), and Mg# ranging from 64 to 72, with or without slight reverse zoning. More abundant than clinopyroxene
Clinopyroxene	(< 7-13 vol.%) are euhedral and very homogeneous phenocrysts and microphenocrysts displaying homogeneous augitic compositions (En40-43, Fs13-17, Wo41-45), with no chemical zonation (Fig. 11b). Clinopyroxene is extremely rare or absent in the pumiceous samples as well as in the whitish andesitic blocks of the PDC deposits.
Fe-Ti oxides	(< 5%) appear as microlites and microphenocryts as well as inclusions in most phenocrysts. They are titano-magnetites crystals with a TiO_2 content ranging from 9 to 13 wt.%.
Olivine	(3-5% vol.%) is an accessory phase, especially in some blocks and bombs of the PDC deposits, and display homogeneous and low-MgO compositions (Fo67-75). It shows subhedral habits and common disequilibrium textures (i.e. reaction rims, Fig. 11d)
Amphibole	(5-15 vol.%) appears only in the white pumice samples and is classified as tschermakitic- and magnesio-hornblende. Crystals are non-altered phenocrysts, without any breakdown reaction rims and displaying a narrow compositional range (8.1-9.8 wt.% Al_2O_3, Mg# 59-68, Fig. 11c).
Matrix glass	glass compositions for the scoria and dense juvenile clasts (tephra and PDC) range from 61 to 65 wt.% SiO_2. Matrix glass for the whitish pumice clasts, however, are rhyodacitic to rhyolite in composition ranging from 68 to 76 wt.% SiO_2.

fragmentation due to a phreatomagmatic component. However, that ash could include fine ash suspended in the atmosphere from previous PDCs. Additionally, the low content of lithic clasts together with the morphology and vesicularity of the majority of juvenile clasts indicate that the eruption was essentially magmatic, with little or no involvement of external water.

As stated previously both brown scoria and dark grey juvenile clasts from the fall deposit have a similar whole rock and trace-element compositions. A similar pattern of fall deposits with two distinct juvenile populations of the same composition, with denser clasts in the upper part of the deposit, was described for the 1992 sub-Plinian eruptions of crater Peak, Mount Spurr, in Alaska (Gardner et al. 1998) and also for the larger AD 79 Vesuvius and 1980 Mount St. Helens eruptions (Carey and Sigurdsson 1987; Klug and Cashman 1984). According to Gardner et al. (1998) and Scandone and Giacomelli (2001), the difference in vesicularity between the juvenile clasts was not due to heterogeneities in the magma reservoir but rather to variable ascent rates, decompression and degassing of the magma chamber during the eruptive process.

Comparison with previous Calbuco eruptions

Major eruptive events during historical times at Calbuco volcano occurred in 1792, 1893-1895, 1917, 1929 and 1961.

These eruptions were mainly sub-Plinian events with eruptive columns ~12-15 km high and durations of a few hours for the paroxysmal phase. Between these events other minor eruptions also occurred in 1845, 1906-07, 1911-12, 1932, 1945 and 1972 (Petit-Breuilh 1999). Comparison with previous major eruptions (Petit-Breuilh 1999; Selles and Moreno 2011) suggests that the magnitude and intensity of the 2015 eruption were similar to those of earlier historical events.

There are three main differences that distinguish the 2015 eruption. First, there was a very short period of time (a few hours) between the first unequivocal signals of renewed activity and beginning of the eruptive activity. There was no observed gas release or small explosions, and although low-magnitude seismicity was registered in the previous 3 months, no fumaroles, noises or earthquakes were reported by inhabitants. Previous documented major historical eruptions of Calbuco volcano (1893-1895, 1929, 1961) were characterized by more-prominent precursory signals, such as seismic swarms felt by the inhabitants in surrounding areas and development of fumaroles weeks or months before the main explosive events (Petit-Breuilh 1999). Second, the interval between the two main phases was only a couple of hours, in contrast with typically weeks or months in previous explosive events. Third, the 2015 eruption was characterized only by explosive activity, without emission of lava flows or domes, which had

Table 4 Major and minor element composition for samples from the fallout and PDC deposits from the 22 and 23 April 2015 eruptions from Calbuco volcano

Sample No.	KAL 3A	KAL 3B	KAL 11A	KAL 11B	KAL 17A	KAL 17B	KAL 18	KAL 22B	KAL 17C	KAL 19B	KAL 21
Unit	2015 Tephra fallout	2015 Tephra fallout	2015 Tephra fallout	2015 Tephra fallout	2015 Tephra fallout	2015 Tephra fallout	2015 PDC	2015 PDC	2015 Tephra fallout	2015 PDC	2015 PDC
Subunit	1	3	1	3	1	3	I	B	3	B	I
Clast type	scoria lapilli	dense lapilli	scoria lapilli	dense lapilli	scoria lapilli	dense lapilli	andesitic bomb	andesitic bomb	pumiceous lapilli	pumiceous bomb	siliceous block
SiO2	54.71	54.72	55.36	54.49	55.42	55.10	55.32	55.19	56.27	55.94	55.20
TiO2	0.93	0.90	0.87	0.92	0.88	0.90	0.87	0.89	0.81	0.81	0.76
Al2O3	18.83	18.96	19.16	18.94	18.78	18.77	18.91	18.76	18.75	18.71	19.32
Fe2O3*	8.74	8.58	8.09	8.61	8.47	8.59	8.39	8.59	8.16	8.27	8.45
MnO	0.15	0.15	0.14	0.15	0.15	0.15	0.15	0.15	0.15	0.15	0.15
MgO	4.02	4.05	3.57	4.09	3.76	3.94	3.80	3.88	3.62	3.79	3.67
CaO	8.10	8.18	8.11	8.30	7.97	8.16	8.06	8.13	7.72	7.88	8.18
Na2O	3.72	3.67	3.87	3.73	3.79	3.65	3.73	3.66	3.71	3.65	3.51
K2O	0.64	0.63	0.66	0.62	0.62	0.59	0.61	0.60	0.67	0.64	0.55
P2O5	0.16	0.15	0.17	0.15	0.15	0.15	0.15	0.15	0.16	0.16	0.20
Total	100.00	100.00	100.00	100.00	100.00	100.00	100.00	100.00	100.00	100.00	100.00
Sc	22.87	22.17	20.89	22.86	22.14	23.05	21.46	22.55	19.63	20.46	18.39
V	187.25	179.56	165.10	190.34	186.19	193.55	182.15	195.03	165.27	173.21	155.46
Cr	8.61	8.34	6.85	8.89	8.08	8.30	7.43	8.70	7.77	9.21	7.49
Co	22.31	22.44	19.62	23.01	21.42	22.20	21.86	21.45	20.56	24.07	26.03
Ni	5.39	6.66	7.36	6.28	7.74	7.93	7.72	9.09	7.62	11.57	19.55
Rb	14.64	15.55	15.50	14.16	12.87	12.16	14.09	13.00	15.58	14.52	12.98
Sr	332.83	317.73	335.47	336.04	342.21	340.80	341.93	339.33	342.60	339.95	380.73
Y	20.54	20.82	21.89	20.92	21.77	20.75	21.27	20.44	20.58	20.55	17.19
Zr	83.40	80.15	85.96	80.05	82.89	77.36	80.67	79.72	85.72	83.25	68.33
Nb	3.58	2.95	3.20	4.11	2.94	3.23	2.54	2.41	3.05	2.68	1.54
Ba	155.09	148.85	160.06	149.44	154.94	143.92	152.65	153.58	168.19	161.70	144.82
La	5.81	5.54	5.88	5.62	6.78	6.21	6.73	6.62	7.32	6.91	6.27
Ce	14.56	16.02	16.40	14.91	16.01	15.43	18.01	17.77	18.52	16.87	16.77
Nd	10.64	10.73	11.34	11.35	11.89	11.34	11.53	11.17	11.61	11.90	10.25
Sm	2.81	2.82	3.04	3.03	2.60	2.53	3.04	2.70	3.13	3.04	2.37
Eu	0.97	1.05	1.02	1.01	1.07	0.93	1.02	1.04	1.01	1.01	0.96
Gd	3.24	3.41	3.39	2.99	3.99	3.62	3.57	3.65	3.73	3.41	3.02
Dy	3.25	3.10	3.58	3.25	3.60	3.46	3.50	3.39	3.30	3.36	2.93
Er	1.77	1.24	1.66	2.21	2.34	2.02	2.09	2.36	2.07	2.20	1.83
Yb	2.02	1.90	2.09	1.99	2.20	2.06	2.14	2.06	2.07	2.03	1.71
Th	0.84	0.80	1.02	1.02	0.97	0.86	0.89	0.98	0.98	1.06	0.88

Sample No.	KAL-21bis	KAL-60A	KAL-60D	KAL-60E2	KAL-64H	KAL-64I	KAL-62G	KAL-62G1	KAL-20
Unit	2015 PDC	2015 PDC	2015 PDC	2015 PDC	2015 PDC	2015 PDC	2015 PDC	2015 PDC	1961 lava flow
Subunit	I	G	F	E	B	A	C	C	
Clast type	siliceous block	andesitic bomb	andesitic bomb	andesitic bomb	andesitic bomb	andesitic bomb	(withish) andesitic bomb	andesitic bomb	lava block
SiO2	55.29	55.32	55.03	55.21	55.31	55.37	58.07	55.45	55.43
TiO2	0.73	0.87	0.90	0.89	0.88	0.88	0.69	0.91	0.85
Al2O3	19.81	18.88	18.84	18.86	18.80	18.81	18.51	18.65	18.89
Fe2O3*	8.11	8.47	8.62	8.61	8.51	8.49	7.67	8.58	8.31

Table 4 (continued)

Sample No.	KAL-21bis	KAL-60A	KAL-60D	KAL-60E2	KAL-64H	KAL-64I	KAL-62G	KAL-62G1	KAL 20
MnO	0.15	0.15	0.15	0.15	0.15	0.15	0.14	0.15	0.15
MgO	3.48	3.87	3.97	3.89	3.92	3.87	3.15	3.90	3.94
CaO	8.31	8.04	8.09	8.03	8.01	7.96	7.09	7.98	8.07
Na2O	3.41	3.64	3.67	3.61	3.67	3.71	3.77	3.65	3.60
K2O	0.56	0.60	0.59	0.60	0.60	0.61	0.76	0.60	0.61
P2O5	0.15	0.15	0.15	0.15	0.15	0.15	0.15	0.15	0.14
Total	100.00	100.00	100.00	100.00	100.00	100.00	100.00	100.00	100.00
Sc	16.69	22.19	22.27	22.35	22.50	22.26	16.06	21.96	22.05
V	150.46	187.04	190.56	190.43	186.78	182.80	132.77	194.77	181.15
Cr	22.22	24.38	24.76	25.50	25.32	24.19	23.04	25.86	10.60
Co	19.24	21.83	23.91	22.37	23.50	22.17	17.29	21.27	21.91
Ni	4.90	8.44	10.01	8.92	7.99	7.28	6.13	8.33	9.23
Rb	15.54	15.88	15.15	17.12	17.68	16.65	21.25	17.50	12.59
Sr	380.39	338.90	340.31	344.53	345.54	339.16	332.49	333.41	337.08
Y	15.46	20.52	19.87	20.28	20.59	20.46	18.58	18.80	20.15
Zr	70.67	80.01	78.47	79.58	80.35	81.33	90.52	77.83	79.07
Nb	3.05	2.89	3.86	3.35	3.48	3.44	3.58	3.03	4.16
Ba	147.06	153.30	147.35	150.23	153.18	154.14	187.57	144.65	154.82
La	6.08	6.76	6.22	6.70	6.52	6.33	7.91	5.70	6.63
Ce	13.73	14.54	16.44	17.14	16.65	15.17	17.49	13.49	15.88
Nd	10.01	11.40	11.69	11.01	11.32	11.67	12.11	10.41	11.53
Sm	2.48	3.07	3.33	3.09	3.11	3.60	2.91	2.83	2.79
Eu	0.87	1.07	1.06	1.04	1.00	0.97	1.00	0.90	1.00
Gd	2.84	3.54	3.13	3.88	3.46	3.89	3.25	3.08	3.72
Dy	2.81	3.64	3.38	3.49	3.44	3.52	3.25	3.42	3.54
Er	1.62	2.71	2.33	2.28	2.02	1.95	2.12	1.53	2.30
Yb	1.64	2.11	2.09	2.14	2.00	2.05	1.99	1.86	2.07
Th	0.76	0.86	0.84	0.67	0.67	0.75	1.24	0.75	1.09

Fig. 12 **a** K$_2$O v/s SiO$_2$ **b** MgO v/s SiO$_2$ **c** Rb v/s SiO$_2$ and **d** La v/s SiO$_2$ for selected samples of the 22-23 April eruptions. The only sample that has a more evolved composition is the whitish highly crystalline block from layer C of the PDC deposits. Also shown (star) 1961 lava flow composition
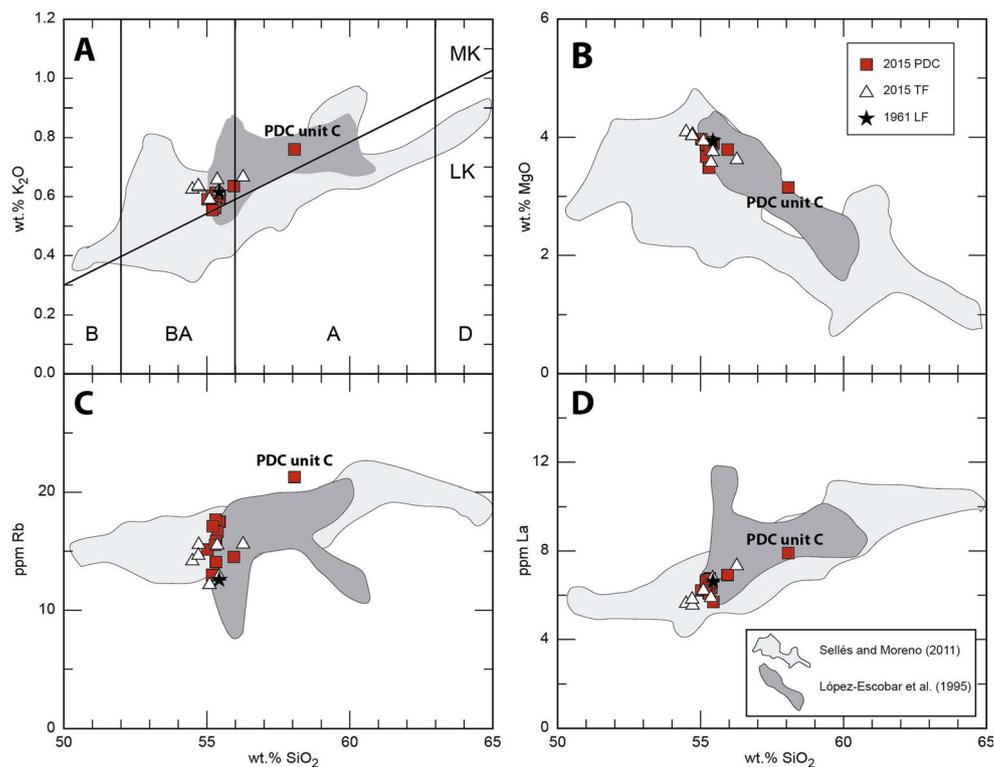
been formed in all previous documented eruptions (Petit-Breuilh 1999).

We suggest that closely spaced eruptive pulses, fast ascent of magma, short duration of the eruption and the occurrence of only explosive activity during the 2015 eruption are consistent with fast ascent of magma from the crustal storage region to the vent. Woods and Koyagushi (1994), Eichelberger (1995) and Slezin (2003) have argued that high ascent velocities of magma prevent the escape of volatiles upwards through the melt or through porous host rock, hence favoring explosive eruptions. Scandone et al. (2007) also argued that pre-eruption VT seismicity is associated to rock fracturing and the developing and interconnection of the conduit network. For the Calbuco eruption, the brief 3-hour swarm of seismic events and the very low magnitude and number of VT events during months before the eruption indicate that the transport system opened quickly and magma ascended at high rates from the moment an overpressure threshold was reached in the magma chamber.

Triggering mechanisms

The sudden start and minimal precursory signals of the 2015 Calbuco eruption raise the question of what were the eruption's triggering mechanisms. Passarelli and Brodsky (2012) reviewed the potential causes for the duration of precursory activity (i.e. the unrest period) and found a positive correlation with repose time and silica content. However, the

repose time before this eruption and composition of the 2015 magma are similar to those of previous eruptions, so these factors cannot explain the shorter unrest period of the 2015 eruption compared with previous ones.

For the 2015 Calbuco eruption we discard earthquake triggering because no major earthquake has been reported in the region for the past five years (Chilean National Seismic Center, www.sismologia.cl). We also discard magma-water interactions as a triggering mechanism; we show in previous sections that the tephra fall deposits have a low abundance of fine-grained tephra and scarce lithic fragments, typical of products from magmatic eruptions. Our data suggests that large scale magma mixing is also very unlikely because the composition of the emitted products is very homogeneous (with the exception of the highly crystalline blocks from unit C of the PDCs). There is some macroscopic textural heterogeneity (banding, enclaves; Fig. 6c, d) but with same (± 1 wt.% SiO$_2$) chemical composition. The abundance of mineral disequilibrium textures and reverse zoning is also very low. In addition, according to White and McCausland (2016), the low seismic energy released by the precursory activity supports the hypothesis of little or no magma injection.

Our data suggest that a likely mechanism for triggering of the 2015 Calbuco eruption is volatile oversaturation, which built-up overpressure inside the magma chamber and caused the eruption. Preliminary microprobe results on amphiboles indicate a high content of water (4-5%) in the magma, and pressures of 180-240 MPa (Ridolfi and Renzulli 2012, see Supplementary

Material 1), together implying oversaturation of water (Baker and Alletti 2012) for a basaltic andesite magma, although amphiboles are only present in the white pumices that represent a very small (<1 vol.%) fraction of the eruptive products. Volatile oversaturation can be caused by crystallization of anhydrous minerals (e.g. Stix et al. 1997), by the exsolution of volatiles from a cooling injection at the base of a magma chamber (Folch and Martí 1998) or by a decompression event such as volcano edifice failure (Scandone and Giacomelli 2001).

There was no obvious decompression event, so the most probable options are the first two. Eruption triggering by differentiation and volatile oversaturation in a closed system was first investigated by Blake (1984) for silica-rich systems. Later, Tait et al. (1989) and Stix et al. (1997) analyzed basaltic and andesitic magmatic systems respectively, showing that low degrees of crystallization (< 10%) can generate the necessary overpressure, depending on the depth of the magma chamber.

The second option is that the triggering mechanism was a small intrusion of magma that did not significantly mix with the host magma, or that had a composition close to that of the magma resident at the base of the chamber. This intrusion would have not led to extensive magma mixing but may have heated the base of the chamber, as shown by rare disequilibrium textures and reverse zoning in minerals (Fig. 11a). The arrival of magma at the base of the reservoir generated overpressure because volatiles were exsolved from the intruded magma (Folch and Martí 1998). This intrusion process may provoke convection and mobilization of different parts of the chamber with different degrees of crystallinity (Fig. 13a) as evidenced by the eruption of clasts with different textures such as white pumices and the very crystalline white blocks from the deposit C of the PDCs.

In either case, the exsolution of volatiles generated an overpressure inside the magma chamber (Fig. 13a), triggering the first phase of the eruption. The eruption of the first batch of magma (Fig. 13b) started to decompress the chamber, causing further vesiculation (Scandone and Giacomelli 2001). However, because of the short duration of the first phase, we suggest that the decompression due to the evacuation of magma was faster than the nucleation of bubbles, causing the first eruption phase to stop.
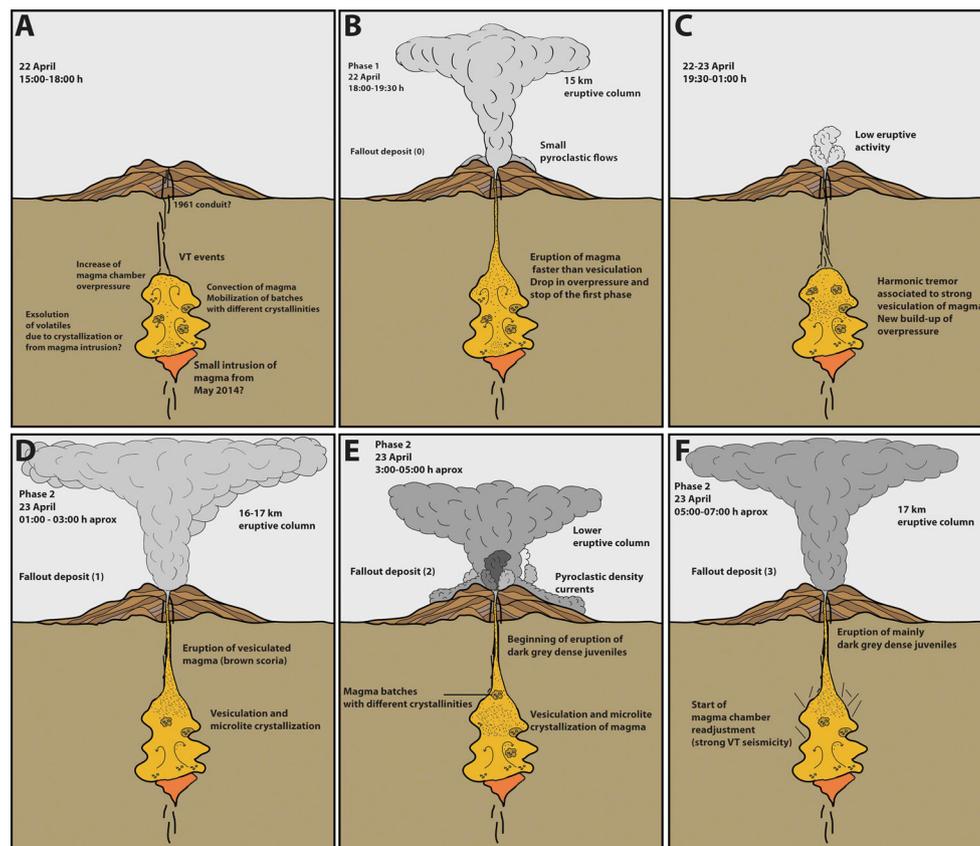
Fig. 13 Cartoon (not to scale) showing the evolution of the April 2015 eruption. **a** Crystallization or a small intrusion of magma produces exsolved volatiles, with generation of convection and vesiculation of the intruded magma that increase the overpressure. **b** The overpressure triggers the first eruption, decompressing the chamber and producing strong vesiculation of the upper part of the chamber. **c** After the end of the first phase, strong vesiculation and crystallization occur in response to depressurization after evacuation of first-phase magma, increasing the overpressure again. **d** The second phase starts with higher eruption rate than the first phase. **e** As vesiculation continues, dark-grey dense clasts begin to be erupted, with a lower eruptive column and major occurrence of PDCs. **f** Eruption rate increases again and a stable eruptive column is reestablished. Dark-grey clasts dominate the erupted products. Sudden stop of the eruption. Strong VT seismicity signals the readjustment of the magma chamber

During the 5.5 hours hiatus between phases, vesiculation inside the chamber became more vigorous (Fig. 13c), signaled by strong harmonic tremor (Scandone and Giacomelli 2001; McNutt et al. 2015). The tiny, Na-rich overgrowth rims observed on plagioclase phenocryst suggest a decompression-induced degassing process occurring just before the eruption (Crabtree and Lange 2011). Experimental studies suggest that a 1-2 wt.% decrease in water contents of siliceous magmas can result in lowering the An content of plagioclase by tens of mole percent. (Couch et al. 2001, Waters and Lange 2015). This vesiculation increased the overpressure inside the chamber up to a threshold value that triggered the second phase. This second phase started with a stronger eruption rate, as vesiculation reached higher degrees (Fig. 13d). As the eruption continued, higher degrees of exsolution promoted the crystallization of microlites, increasing the viscosity of magma and inhibiting the growth of vesicles, hence provoking an increase in the proportion of dark-grey dense juveniles. The eruption rate during this transitional stage was lower (Fig. 13e), but the continuous vesiculation of magma in the reservoir favored a new increase in eruption intensity (Scandone and Giacomelli 2001) towards the end of this phase, with a return to a sustained column again (layer 3, Fig. 13f). VT events towards the end and after the second phase probably reflected readjustment of the magma chamber. After the end of the second phase, the magma chamber was highly degassed and (partially) emptied, generating only small eruptions that lasted for a couple of weeks.

Conclusions

The Calbuco volcano eruption of April 22-23, 2015 was marked by two sub-Plinian events that generated eruptive columns of 15-17 km height with a NE dispersion axis and a total erupted volume of 0.15 km^3 (DRE). Pyroclastic density currents produced only ~10% of the total deposit volume and reached distances of up to 6 km. Despite the wide range in textures of clasts emitted during the eruption, most of the eruption products are basaltic andesite in composition. The eruption was preceded by scarce seismicity, which together with the homogenous composition and lack of reverse zoning and disequilibrium textures in minerals, argues against magma mixing as a triggering mechanism of the eruption. Instead, we propose that the eruption could have been triggered by volatile oversaturation, probably enhanced by crystallization or volatile addition from a small intrusion without significant mixing or with the same composition as the main body of magma. This caused over-pressurization of the system, which favored fracturing of the surrounding rock and opening of a conduit to the surface, thus causing the onset of the first eruptive phase. This phase lasted 1.5 hours. After a pause of 5.5 hours, a second phase began and was marked by a stronger intensity at its beginning. Nearly 2 hours after the start of the second phase, the eruption rate decreased and widespread PDCs were

generated possibly due to the abundance of denser fragments (dark grey dense juvenile clasts) in the column. This second phase caused more decompression and vesiculation inside the chamber, thus increasing microlite crystallization and bubble nucleation, and culminated with a sustained eruptive column that reached a height of 17 km at the end of the eruption. The eruption ended abruptly after 6 hours of almost continuous activity.

References

Baker DR, Alletti M (2012) Fluid saturation and volatile partitioning between melts and hydrous fluids in crustal magmatic systems: the contribution of experimental measurements and solubility models. Earth Sci Rev 114:298–324

Bertin D, Amigo A, Mella M, Astudillo V, Bertin L, Bucchi F (2015) Erupción del volcán Calbuco 2015: Estratigrafía eruptiva y volumen involucrado. XIV Congreso Geológico Chileno, La Serena, Abstracts

Blake S (1984) Volatile oversaturation during the evolution of silicic magma chambers as an eruption trigger. J Geophys Res 89:8237–8244

Bonadonna C, Costa A (2012) Estimating the volume of tephra deposits: A new simple strategy. Geology 40:415–418. doi:10.1130 /G32769.1

Bonadonna C, Houghton BF (2005) Total grainsize distribution and volume of tephra-fall deposits. Bull Volcanol 67:441–456

Carey SN, Sparks RSJ (1986) Quantitative models of the fallout and dispersal of tephra from volcanic eruption columns. Bull Volcanol 48:109–125

Castruccio A, Clavero J (2015) Lahar simulation at active volcanoes of the Southern Andes: implications for hazard assessment. Nat Hazards 77:693–716. doi:10.1007/s11069-015-1617-x

Castruccio A, Clavero J, Rivera A (2010) Comparative study of lahars generated by the 1961 and 1971 eruptions of Calbuco and Villarrica volcanoes, Southern Andes of Chile. J Volcanol Geotherm Res. doi:10.1016/j.volgeores.2009.12.005

Clavero J, Godoy E, Arancibia G, Rojas C, Moreno H (2008) Multiple Holocene sector collapses at Calbuco volcano, Southern Andes. Proceedings of the IVACEI General Assembly 2008-Iceland

Clavero J, Castruccio A, Droguett B, Segura A, Le Pennec JL, Roche O, Samaniego P (2015) Small volumepyroclastic density currents of the 22–23 April 2015 eruption on the NE flank of Calbuco volcano, Southern Andes. XIV Congreso Geológico Chileno, La Serena. Abstracts.

Couch S, Sparks RSJ, Carroll MR (2001) Mineral disequilibrum in lavas explained by convective self-mixing in poen magma chambers. Nature 411:1037–1039

Crabtree S, Lange R (2011) Complex PhenocrystTextures and Zoning Patterns in Andesites and Dacites: Evidence of Degassing-Induced Rapid Crystallization? J Petrol 52(1):3–38

Eichelberger JC (1995) Silicic volcanism: ascent of viscous magmas from crustal reservoirs. Annu Rev Earth Planet Sci 23:41–63

Fierstein J, Nathenson M (1992) Another look at the calculation of fallout tephra volumes. Bull Volcanol 54:156–167

Folch A, Martí J (1998) The generation of overpressure in felsic magma chambers by replenishment. Earth Planet Sci Lett 163:301–314

Gardner CA, Cashman KV, Neal CA (1998) Tephra-fall deposits from the 1992 eruption of Crater Peak, Alaska: implications of clast textures for eruptive processes. Bull Volcanol 59:537–555

Inman D (1952) Measures for describing the size distributions of sediments. J Sediment Petrol 22:125–145

Jessop DE, Kelfoun K, Labazuy P, Mangeney A, Roche O, Tillier JL, Trouillet M, Thibault G (2012) LiDAR derived morphology of the 1993 Lascar pyroclastic flow deposits, and implication for flow dynamics and rheology. J Volcanol Geotherm Res 245–246:81–97

Klug C, Cashman K (1984) Vesiculation of May 18, 1980, Mount St. Helens magma. Geology 22:468–472

López L, Parada MA, Moreno H, Frey F, Hickey-Vargas R (1992) A contribution to the petrogenesis of Osorno and Calbuco volcanoes, Southern Andes (41°00'-41°30'S): comparative study. Rev Geol Chile 19:211–226

McNutt S, Thompson G, Johnson J, De Angelis S, Fee D (2015) Seismic and infrasonic monitoring. In: (ed-in-chief) Sigurdsson H. Encyclopedia of Volcanoes (2 ed). Academic press

Mella M, Moreno H, Vergés A, Quiroz D, Bertin L, Basualto D, Bertin D, Garrido N (2015) Productos volcánicos, impactos y respuesta a la emergencia del ciclo eruptivo abril-mayo (2015) del volcán Calbuco. XIV Congreso Geológico Chileno, La Serena. Abstracts

Newhall C, Self S (1982) The volcanic explosivity Index (VEI); An estimate of explosive magnitude for historical volcanism. J Geophys Res 87:1231–1238

Passarelli L, Brodsky E (2012) The correlation between run-up and repose times of volcanic eruptions. Geophys J Int 188:1025–1045. doi:10.1111/j.1365-246X.2011.05298.x

Petit-Breuilh M (1999) Cronología eruptiva histórica de los volcanes Osorno y Calbuco, Andes del Sur (41°-41°30'S). Boletín No. 53, Servicio Nacional de Geología y Minería, Chile, 46 p.

Pyle DM (1989) The thickness, volume and grainsize of tephra fall deposits. Bull Volcanol 51(1):1–15

Pyle DM (2000) Sizes of volcanic eruptions. In: Sigurdsson H, Houghton B, Rymer H, Stix J, McNutt S (eds) Encyclopedia of volcanoes. Academic, San Diego, pp. 263–270

Ridolfi F, Renzulli A (2012) Calcic amphiboles in calc-alkaline and alkaline magmas: thermobarometric and chemometric empirical equations valid up to 1,130°C and 2.2 GPa. Contrib Mineral Petrol 163: 877–895. doi:10.1007/s00410-011-0704-6

Romero JE, Morgavi D, Arzilli F, Daga R, Caselli A, Reckziegel F, Viramonte J, Díaz-Alvarado J, Polacci M, Burton M, Perugini D (2016) Eruption dynamics of the 22–23 April 2015 calbuco volcano (Southern Chile): Analyses of tephra fall deposits. J Volcanol Geotherm Res. doi:10.1016/j.jvolgeores.2016.02.027

Scandone R, Giacomelli L (2001) The slow boiling of magma chambers and the dynamics of explosive eruptions. J Volcanol Geotherm Res 110:121–136

Scandone R, Cashman KV, Malone SD (2007) Magma supply, magma ascent and the style of volcanic eruptions. Earth Planet Sci Lett 253: 513–529. doi:10.1016/j.epsl.2006.11.016

Segura A, Castruccio A, Clavero J, Le-Pennec JL, Roche O, Samaniego P, Droguett B, Romero J (2015) Fallout deposits of the 22-23 April 2015 eruption of Calbuco volcano, Southern Andes. XIV Congreso Geológico Chileno, La Serena Abstracts

Sellés D, Moreno H (2011) Geología del volcán Calbuco. Carta Geológica de Chile, Serie Geología Básica No. 130, escala 1: 50.000.

SERNAGEOMIN (2014a) Reporte Especial de Actividad Volcánica (REAV) Región de los Lagos. Año 2014 Mayo 20:45 HL

SERNAGEOMIN (2014b) Reporte de Actividad Volcánica (RAV) Región de los Lagos. Año 2014 Diciembre. Volumen 2

SERNAGEOMIN (2015a) Reporte de Actividad Volcánica (RAV) Región de los Lagos. Año 2015 Enero. Volumen 1

SERNAGEOMIN (2015b) Reporte de Actividad Volcánica (RAV) Región de los Lagos. Año 2015 Febrero. Volumen 2

SERNAGEOMIN (2015c) Reporte de Actividad Volcánica (RAV) Región de los Lagos. Año 2015 Marzo. Volumen 3

SERNAGEOMIN (2015d) Reporte Especial de Actividad Volcánica (REAV) Región de los Lagos. Año 2015 Abril 22

SERNAGEOMIN (2015e) Reporte Especial de Actividad Volcánica (REAV) Región de los Lagos. Año 2015 Abril 22 (18:00 HL)

SERNAGEOMIN (2015f) Reporte Especial de Actividad Volcánica (REAV) Región de los Lagos. Año 2015 Abril 22 (20:45 HL)

SERNAGEOMIN (2015g) Reporte Especial de Actividad Volcánica (REAV) Región de los Lagos. Año 2015 Abril 22 (22:30 HL)

SERNAGEOMIN (2015h) Reporte Especial de Actividad Volcánica (REAV) Región de los Lagos. Año 2015 Abril 23 (01:10 HL)

SERNAGEOMIN (2015i) Reporte Especial de Actividad Volcánica (REAV) Región de los Lagos. Año 2015 Abril 23 (10:30 HL)

SERNAGEOMIN (2015j) Reporte Especial de Actividad Volcánica (REAV) Región de los Lagos. Año 2015. 29 Abril – 1 Mayo

Slezin YB (2003) The mechanism of volcanic eruptions (a steady state approach), J. Volcanol Geotherm Res 122:7–50

Stern C, Moreno H, Lopez-Escobar L, Clavero J, Lara L, Naranjo J, Parada M, Skewes M (2007) Chilean Volcanoes. In: Moreno T, Gibbons W (eds) The Geology of Chile. Geological Society of London, London, pp. 149–180

Carey S, Sigurdsson H (1987) Temporal variations in column height and magma discharge rate during the 79 A.D. eruption of Vesuvius. Geol Soc Am Bull 99 (2):303

Stix J, Torres R, Narváez L, Cortés G, Raigosa J, Gómez D, Castonguay R (1997) A model of vulcanian eruptions at Galeras volcano, Colombia. J Volcanol Geotherm Res 77:285–303

Tait S, Jaupart C, Vergniolle S (1989) Pressure, gas content and eruption periodicity of a shallow, crystallising magma chamber. Earth Planet Sci Lett 92:107–123

Valderrama O, Franco L, Gil-Cruz F (2015) Erupción intempestiva del volcán Calbuco, abril 2015. XIV Congreso Geológico Chileno, La Serena. Abstracts

Van Eaton A, Amigo A, Bertin D, Mastin L, Giacosa R, González J, Valderrama O, Fontijn K, Behnke S (2016) Volcanic lightning and plume behavior reveal evolving hazards during the April 2015 eruption of Calbuco volcano, Chile. Geophys Res Lett 43. doi:10.1002/2016GL068076

Walker W (1971) Grain-size Characteristics of pyroclastic deposits. J Geol 79:696–714

Waters L, Lange R (2015) An updated calibration of the plagioclase-liquid hygrometer-thermometer applicable to basalts through rhyolites. Am Mineral 100:2172–2184

White R, McCausland W (2016) Volcano-tectonic earthquakes: A new tool for estimating intrusive volumes and forecasting eruptions. J Volcanol Geotherm Res 309:139–155

Wilson L, Walker GPL (1987) Explosive volcanic-eruptions.6. Ejecta dispersal in plinian eruptions—the control of eruption conditions and atmospheric properties. Geophys J R Astron Soc 89(2):657–679

Woods AW, Koyaguchi T (1994) Transitions between explosive and effusive eruption of silicic magmas. Nature 370:641–645